



Article

High-Temperature Corrosion Behavior of $\text{Bi}_{3.75}\text{La}_{0.25}\text{Ti}_3\text{O}_{12}$ and $\text{Bi}_3\text{La}_1\text{Ti}_3\text{O}_{12}$ Coating Prepared by rf Magnetron Sputtering

Jorge Bautista-Ruiz ^{1,*}, Jorge Sánchez-Molina ¹ and Willian Aperador ²

¹ Centro de Investigación de Materiales Cerámicos, Universidad Francisco de Paula Santander, San Jose de Cucuta 540003, Colombia

² Department of Engineering, Universidad Militar Nueva Granada, Bogota 110111, Colombia

* Correspondence: jorgebautista@ufps.edu.co; Tel.: +57-313-852-9876

Abstract: Using the rf magnetron sputtering technique, $\text{Bi}_{3.75}\text{La}_{0.25}\text{Ti}_3\text{O}_{12}$ and $\text{Bi}_3\text{La}_1\text{Ti}_3\text{O}_{12}$ coatings were formed and obtained as a thin film on Hastelloy substrates. When subjected to high-temperature conditions, the effect of lanthanum on the anti-corrosive properties of the coatings was investigated. The anti-corrosive response was evaluated by electrochemical impedance spectroscopy and potentiodynamic curves, which are rarely reported. Hot corrosion occurs through the electrochemical mechanism, and more information can be obtained through electrochemical corrosion tests, which are very effective and fast. The electrochemical behavior at high temperatures was studied via molten salt corrosion tests, potentiodynamic polarization curves, and electrochemical impedance spectroscopy. Additionally, the coatings were evaluated via scanning electron microscopy and transmission microscopy to determine their morphology. With X-ray diffraction, the crystallinity of the films was determined. It was determined that the corrosion rate directly correlates with the temperature, attributed to the mechanisms induced by the Na_2SO_4 and V_2O_5 salts that generated condensation. As the temperature increases, the density of the corrosion current increases in the thin films of $\text{Bi}_{3.75}\text{La}_{0.25}\text{Ti}_3\text{O}_{12}$ and $\text{Bi}_3\text{La}_1\text{Ti}_3\text{O}_{12}$. When comparing the two compounds, it is determined that the increase in lanthanum alters the positive acid character, thus reducing the dissolution of the oxides and increasing protection.

Keywords: hot corrosion; lanthanum doped; accelerated oxidation



Citation: Bautista-Ruiz, J.; Sánchez-Molina, J.; Aperador, W. High-Temperature Corrosion Behavior of $\text{Bi}_{3.75}\text{La}_{0.25}\text{Ti}_3\text{O}_{12}$ and $\text{Bi}_3\text{La}_1\text{Ti}_3\text{O}_{12}$ Coating Prepared by rf Magnetron Sputtering. *Metals* **2022**, *12*, 1585. <https://doi.org/10.3390/met12101585>

Academic Editor: Jordi Sort Viñas

Received: 10 August 2022

Accepted: 20 September 2022

Published: 23 September 2022

Publisher's Note: MDPI stays neutral with regard to jurisdictional claims in published maps and institutional affiliations.



Copyright: © 2022 by the authors. Licensee MDPI, Basel, Switzerland. This article is an open access article distributed under the terms and conditions of the Creative Commons Attribution (CC BY) license (<https://creativecommons.org/licenses/by/4.0/>).

1. Introduction

The composite of bismuth, titanium, and oxygen in the $\text{Bi}_4\text{Ti}_3\text{O}_{12}$ phase is a material that contributes to the phase-structured ferroelectrics family [1]; it consists of three units of a perovskite-like structure. It has a high dielectric constant and high breakdown strength; the high Curie temperature is reported to be 675 °C [2], making it useful for applications as a converter for pyro-electric devices over a wide temperature range (20 to 600 °C). $\text{Bi}_4\text{Ti}_3\text{O}_{12}$'s perovskite structure comprises three layers of TiO_6 octahedra with Bi_3^+ ions. The layers of octahedra and $(\text{Bi}_2\text{O}_2)_2^+$ are observable when Trivalent elements such as lanthanum are used to replace bismuth [3,4]. Bi_2O_3 applications have been primarily used in sensors and solid electrolytes [5,6]. However, there is a broad spectrum of applications for bismuth-based ternary and quaternary compounds containing metal oxides, and uses have been found in areas such as pigments, superconductors, sensors, scintillators, oxidation catalysis, photocatalysis, high-temperature electrolytes, and thermal barrier materials [7].

Technological advances allow the development of coatings for applications in high-performance devices, where they are deposited on metal parts exposed to high temperatures and corrosive environments [8]. In the process of high-temperature corrosion, the degradation of materials does not require the presence of a liquid electrolyte [9]. In most industrial environments, high-temperature oxidation, regardless of the predominant mode of corrosion, has demanded the development of materials and techniques to match its needs for

device fabrication [10], leading to the research and production of materials in particular designs and arrangements. The corrosion rate depends on the physicochemical properties of the material, the corrosive atmosphere in which it is exposed, and the corrosion products [11]. In a variety of engineering application systems where high temperatures are used, contact between the material and the molten salt film occurs, generating a considerable increase in the corrosion rate of the materials and thus causing their deterioration [12]. High-temperature corrosion phenomena, due to salt deposits caused by combustion ashes, have usually resulted in the modification of the reaction rate of the metal with the environment. This produces molten salt baths or salt films with high adhesion to be in contact with the metal at elevated temperatures [13].

Consequently, there is an acceleration of corrosion that often occurs on the contact of the molten salt electrolyte with the metal or its protective oxide film. It is evident, then, that the combustion of ash is a significant factor in the corrosive attack. Sodium sulfate (Na_2SO_4) and vanadium pentoxide (V_2O_5) are the most common salts in deposits involved in molten salt corrosion and come from fuels containing contaminants such as sulfur (S) and vanadium (V), or in environments that may contain sodium chloride (NaCl) [14]. When fuels are burned with excess oxygen, Na_2SO_4 , V_2O_5 , and NaVO_3 , among others, are formed. Vanadium-containing substances are very harmful and contribute to increased corrosion in combustion process equipment. Since many studies have been carried out to examine the mechanisms of Na_2SO_4 -induced hot corrosion, researchers have found that the condensation of Na_2SO_4 is necessary to accelerate corrosion [15].

In this study, rf magnetron sputtering was used to fabricate coatings. Hot corrosion occurs through the electrochemical mechanism, and more information can be obtained through electrochemical corrosion testing, which is very effective and quick [16]. Electrochemical impedance spectroscopy (EIS) is a technique that has proven effective in investigating the mechanisms and reaction kinetics in hot corrosion induced by molten carbonates. Electrochemical testing of the Tafel determination of the corrosion rate was performed using a method known as Tafel extrapolation [17]. As with all electrochemical studies, the environment must be electrically conductive. Although potentiodynamic curves and electrochemical impedance spectroscopy measurements are widely used to evaluate the corrosion resistance or reveal the corrosion mechanism at room temperature [18], electrochemical measurements are rarely used at high temperatures. In this study, high-temperature corrosion behavior was measured by electrochemical impedance spectroscopy measurements and potentiodynamic curves [19,20].

2. Materials and Methods

$\text{Bi}_{3.75}\text{La}_{0.25}\text{Ti}_3\text{O}_{12}$ and $\text{Bi}_3\text{La}_1\text{Ti}_3\text{O}_{12}$ thin films on commercial Hastelloy X Nickel-based superalloy substrates were fabricated by rf magnetron sputtering. The details of the deposition process and conditions were as follows: $\text{Bi}_{3.75}\text{La}_{0.25}\text{Ti}_3\text{O}_{12}$ and $\text{Bi}_3\text{La}_1\text{Ti}_3\text{O}_{12}$ targets [15], rf power of 40 W, argon deposition atmosphere, deposition time 65 min, target to substrate distance 65 mm. Samples were ultrasonically cleaned in acetone for 15 min before the X-ray diffraction (XRD) and scanning electron microscopy (SEM) characterization. Coating surfaces and their cross-sections were examined with the JSM 6490LV JEOL SEM to determine the morphological and microstructural modifications before and after the hot corrosion treatment. X-ray diffraction (XRD) was used for local element analyses, and for detecting corrosion products both on the surface and throughout the thickness of the sample. These coatings were structurally characterized by XRD before and after the hot corrosion test and analyzed by Rietveld's method. X-ray diffraction patterns were collected at room temperature using 0.0197° (2θ) scanning steps over a range of $9.9972^\circ < 2\theta < 90.00001^\circ$ on a Panalytical X'Pert Pro MRD with $\text{Cu K}\alpha$ (1.541874 \AA) radiation.

For electrochemical impedance spectroscopy measurements and potentiodynamic curves, the sample was placed in an induction furnace and heated from room temperature to a maximum of 1000°C . Measurements were made at three temperatures: $700 \pm 3^\circ\text{C}$, $850 \pm 3^\circ\text{C}$, and $1000 \pm 3^\circ\text{C}$. These temperatures were maintained for 45 min in an

air atmosphere while electrochemical measurements were performed. Afterward, the specimen was cooled to room temperature to reduce thermal shocks. The experimental setup for the EIS analysis is presented in Figure 1.

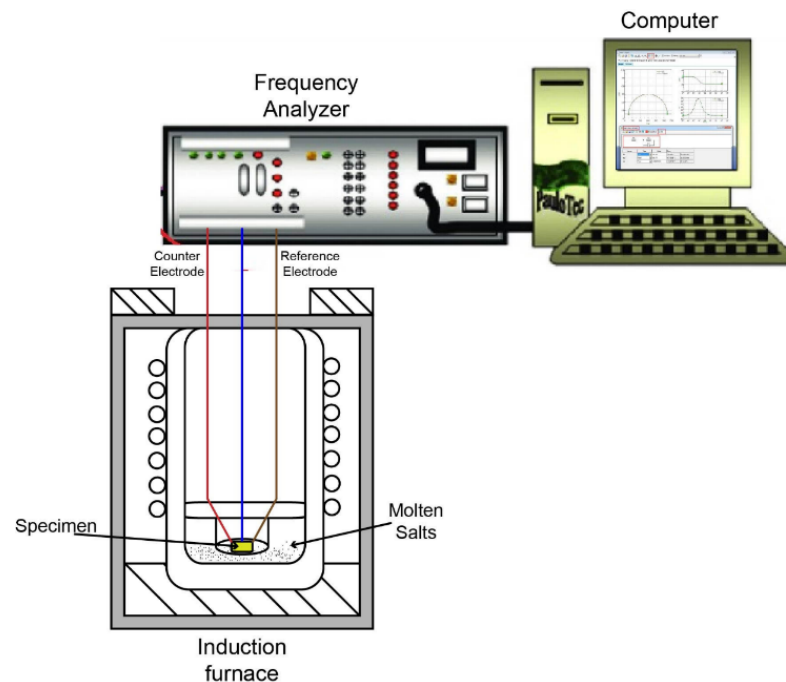


Figure 1. Experimental setup for high-temperature corrosion analysis.

Electrochemical measurements were performed using a Gamry Instrument Interface 1010E potentiostat frequency response analyzer. Electrochemical impedance spectroscopy (EIS) curves were obtained in situ at 700 ± 3 °C, 850 ± 3 °C, and 1000 ± 3 °C, using a cell containing a working electrode with an exposed area of 1 cm^2 , a platinum wire as a counter electrode (CE), and a platinum wire as a reference electrode (RE). In the laboratory conditions, a mixture of vanadium pentoxide powder (V_2O_5) and sodium sulfate (Na_2SO_4) in a ratio of 50:50 (wt%) at a rate of 90 g/cm^2 was used as the corrosive salt for the simulation of the accelerated hot corrosion process. Bode plots were recorded using a sinusoidal signal amplitude of 5 mV applied to the working (specimen) and reference electrodes in a frequency range from 0.1 Hz to 300 kHz. Polarization curves were obtained at a sweep speed of 1 mV/s in a voltage range between -0.25 and 0.25 V against the electrode reference potential, defined for the open-circuit potential.

3. Results and Discussion

3.1. High-Temperature Corrosion

Figure 2 shows the potentiodynamic polarization curves for the substrate as a function of temperatures of 700 °C, 850 °C, and 1000 °C, respectively. Again, the variation of the corrosion potentials is observed. The corrosion potential generally tends to take more positive values at 850 °C. The values of corrosion potential, corrosion current, and corrosion rate for the substrate, according to the heat treatment temperatures, are consolidated in Table 1.

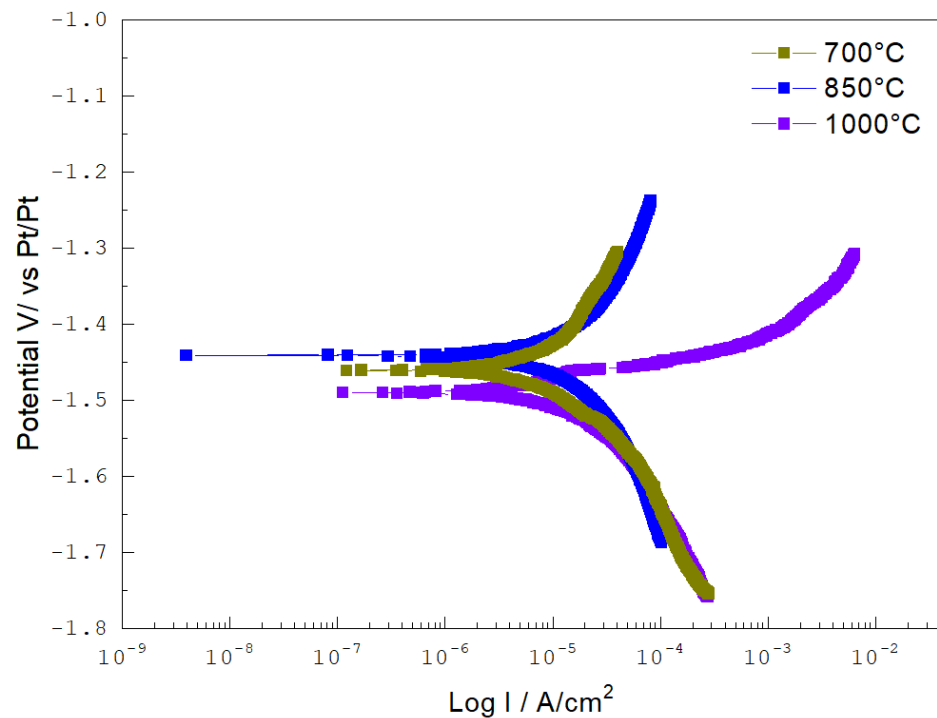


Figure 2. Potentiodynamic curves correspond for the substrate evaluated at 700 °C, 850 °C, and 1000 °C.

Table 1. The corrosion potential, current density, and corrosion rate were obtained for the steel substrate at 700 °C, 850 °C, and 1000 °C.

Temperature (°C)	Error (V vs. Pt)	I _{corr} (μA/cm ²)	Corrosion Rate (μm/Year)
700	−1.47	8.18×10^{-6}	94.28
850	−1.44	16.95×10^{-6}	195.36
1000	−1.49	77.44×10^{-6}	892.55

The responses of the coatings at high temperatures are evaluated by employing two tests; the first one, to determine the rate of corrosion and the corrosion kinetics, is the potentiodynamic polarization technique (Figures 3 and 4). The evaluation of the oxidation of the coatings in molten salts simulates severe conditions in atmospheres, with the presence of contaminants and materials used in pipes that must withstand high temperatures in combustion processes (580 °C) [21,22]. Hence, a coated film aims to protect the base material, which is the same steel previously used for this purpose. Therefore, the degree of protection of the metal–coating interface must be determined. In Figures 2 and 3, the corrosion rate was determined to have a direct relationship with the temperature where the mechanisms induced by the Na₂ SO₄ and V₂O₅ salts have generated condensation. By increasing the temperature, the corrosion current density increases in the thin films of Bi_{3.75}La_{0.25}Ti₃O₁₂ and Bi₃La₁Ti₃O₁₂. By comparing the two compounds, it is determined that the increase in La alters the positive acid character, thus decreasing the dissolution of the oxides and increasing the protection [23]. The concentrations of Titanium are kept constant, and the concentrations of Lanthanum are varied, the results show that increasing the content of Lanthanum in the coatings improves the anticorrosive protection of the substrate, as observed when comparing the potentiodynamic curves. This curve indicates that the electrochemical action involving combustion gases and corrosive salts depends on the compounds formed at the test temperatures. The corrosion rates in the so-called high-temperature elements are engineered in systems with temperatures above 600 °C; the base steel performs adequately under this temperature. However, at temperatures above 700 °C, layers of molten solids are formed, causing an increase in both the corrosion rate

and the deterioration of the substrate. The coating protects the substrate from accelerated corrosion processes [24].

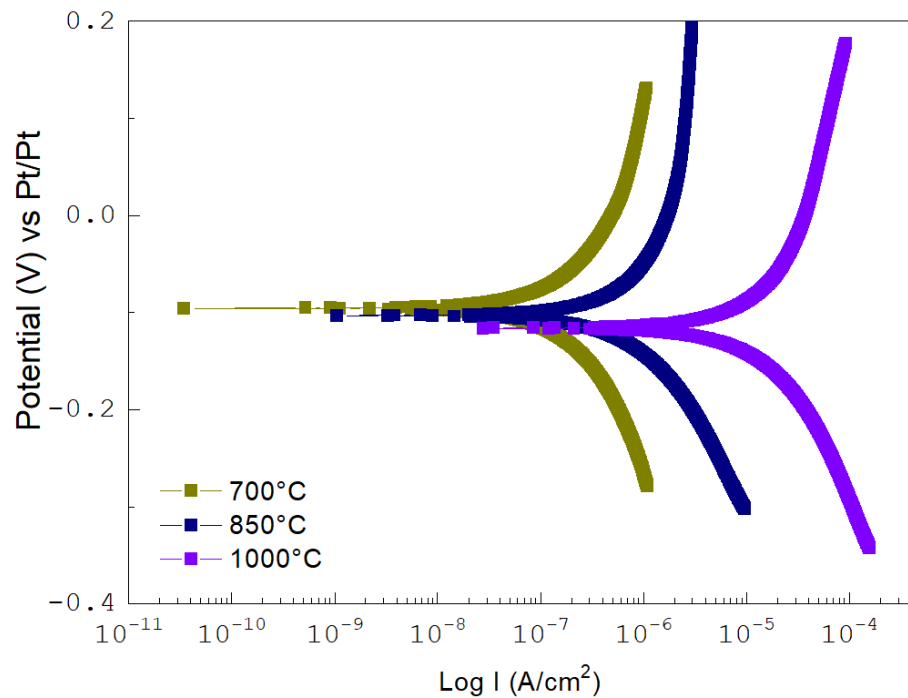


Figure 3. Potentiodynamic curves for $\text{Bi}_{3.75}\text{La}_{0.25}\text{Ti}_3\text{O}_{12}$ coatings evaluated at temperatures of 700 °C, 850 °C and 1000 °C.

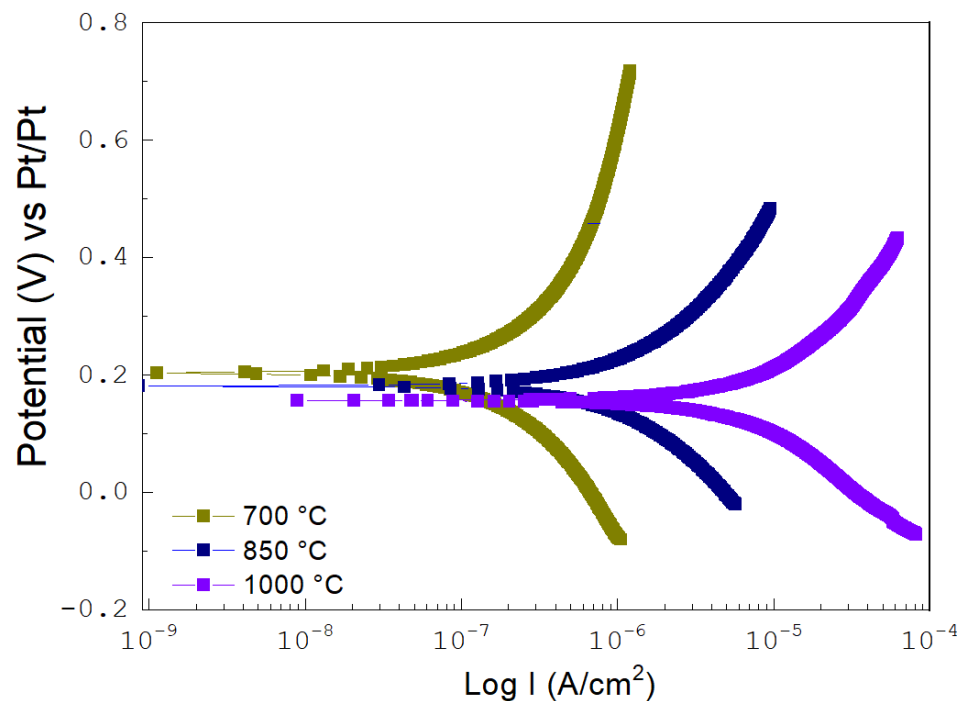


Figure 4. Potentiodynamic curves for $\text{Bi}_3\text{La}_1\text{Ti}_3\text{O}_{12}$ coatings evaluated at temperatures of 700 °C, 850 °C and 1000 °C.

Figures 3 and 4 correspond to the potentiodynamic curves of the $\text{Bi}_{3.75}\text{La}_{0.25}\text{Ti}_3\text{O}_{12}$ and $\text{Bi}_3\text{La}_1\text{Ti}_3\text{O}_{12}$ coatings. The results show that the damage is minimal at temperatures of 700 °C. When increasing to 850 °C, significant damage to the substrate-coating system is

evident. At 1000 °C, damages are catastrophic due to increased corrosion current density. In all the evaluated cases, it was determined that a general dissolution exists in the anodic region. There was no evidence of pitting corrosion, typical of steel, which indicates an adequate barrier. When a general dissolution is generated, this is associated with the thin film having contact with the molten salt composed of vanadium, sodium, and sulfur. The more ashes of these compounds are generated by the evaluation temperature, the more degradation is present, and therefore, these compounds are related to a condensed corrosion-causing phase at high temperatures [25].

The results based on the treatment temperatures, the corrosion potential, current, and corrosion rate values for $\text{Bi}_{3.75}\text{La}_{0.25}\text{Ti}_3\text{O}_{12}$ and $\text{Bi}_3\text{La}_1\text{Ti}_3\text{O}_{12}$ are consolidated in Tables 2 and 3, respectively.

Table 2. The corrosion potential, current density, and corrosion rate obtained for $\text{Bi}_{3.75}\text{La}_{0.25}\text{Ti}_3\text{O}_{12}$ at 700 °C, 850 °C, and 1000 °C.

Temperature (°C)	Error (V vs. Pt)	I _{corr} (μA/cm ²)	Corrosion Rate (μm/Year)
700	−0.09	1.01×10^{-6}	1.12
850	−0.10	0.68×10^{-6}	7.82
1000	−0.11	16.10×10^{-6}	185.55

Table 3. The corrosion potential, current density, and corrosion rate obtained for $\text{Bi}_3\text{La}_1\text{Ti}_3\text{O}_{12}$ at 700 °C, 850 °C, and 1000 °C.

Temperature (°C)	Error (V vs. Pt)	I _{corr} (μA/cm ²)	Corrosion Rate (μm/Year)
700	0.21	0.10×10^{-6}	1.18
850	0.18	0.59×10^{-6}	4.47
1000	0.16	8.14×10^{-6}	93.83

3.2. Electrochemical Impedance Spectroscopy

Figures 5 and 6 present the Bode diagrams, which are the response of the electrochemical impedance spectroscopy technique using 5 mV and a potential signal applied to $\text{Bi}_{3.75}\text{La}_{0.25}\text{Ti}_3\text{O}_{12}$ and $\text{Bi}_3\text{La}_1\text{Ti}_3\text{O}_{12}$ coatings, evaluated in the temperature range of 700 °C to 1000 °C, in 150 °C increments, where these films are undergoing corrosion processes. The response is measured in current, thus determining the material's response to the degradation processes [26]. Bode diagram analysis allows observation by the logarithm of the absolute value of the impedance versus the frequency. In the two systems, it was determined that at high temperatures, the impedance response is low, and as a result, a series of impedance values is obtained for each frequency studied. This relationship between frequency and impedance is known as the impedance spectrum, where the system with the lowest amount of lanthanum response is about 10 ohm (Figure 5).

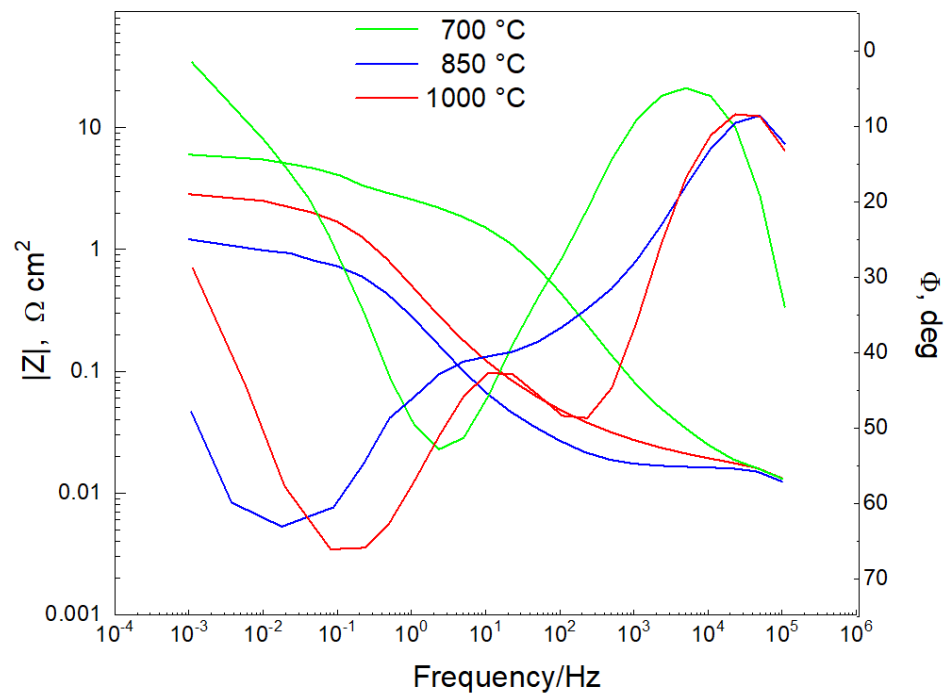


Figure 5. Bode diagram for the $\text{Bi}_{3.75}\text{La}_{0.25}\text{Ti}_3\text{O}_{12}$ composite.

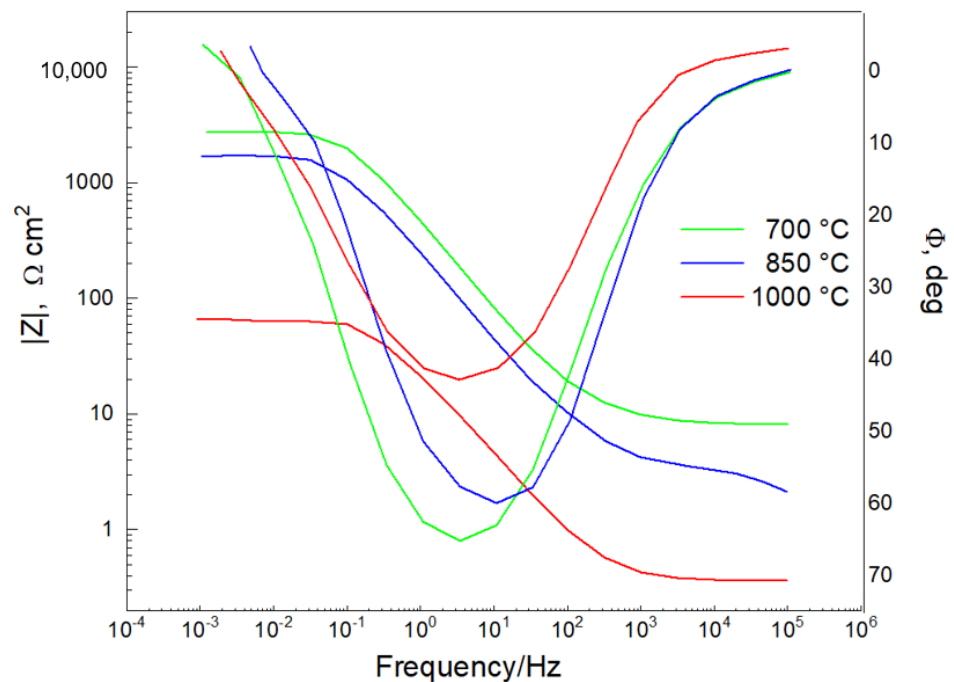


Figure 6. Bode diagram for the $\text{Bi}_3\text{La}_1\text{Ti}_3\text{O}_{12}$ composite.

The system with the highest lanthanum content evaluated at 1000 °C shows a six-fold increase to 67 ohm (Figure 6) [27,28]. These plots indicate similar results for the systems evaluated at 700 °C and 850 °C due to the material's temperature increase. The resulting signals were obtained due to the frequency variation between 10^{-2} Hz and 10^1 Hz, which allowed the diagrams to be adjusted by applying the same input variable to the physical interpretation and the chemical reactions. The diagrams indicate that the generated reactions allow charge transport, i.e., the corrosive salts are transported through the material. As the temperature increases, the rate of charge transport increases; regarding the barrier generated by the formation of a surface coating on the substrates, and the flow

of charge through this protective layer, the Bode diagrams indicate that at both 700 °C and 850 °C the system is suitable. The spectrum does not allow corrosive salts to permeate because of pores that have not interconnected. However, at 1000 °C, these pores interlock and form cracks and can be highly brittle [29]. The phase that generates the protection is due to the characteristics of the bismuth lanthanum titanate thin film. In this case, the composite with a higher amount of lanthanum generates 10 times more protection; however, after surpassing 850 °C, the transfer of charge through the discontinuities and defects of the thin film causes the breakage of the protective layer, resulting in continuous failure [30,31].

The equivalent circuit proposed to model the behavior of the $\text{Bi}_{3.75}\text{La}_{0.25}\text{Ti}_3\text{O}_{12}$ and $\text{Bi}_3\text{La}_1\text{Ti}_3\text{O}_{12}$ coatings has been schematized in Figure 7. The model considers that the corrosion of the films deposited on the substrate is located in the permeable pores where corrosive salts can penetrate them and reach the surface of the substrate. Therefore, the coating can be considered a leaky capacitor (constant phase element). The constituent elements of the electrical circuit in Figure 7 are as follows: R.E. the reference electrode, W.E. the working electrode, R_s solution resistance, R_{p1} porosity charge transfer resistance, CP1 coating capacitance, CP2 the capacitance of the exposed metal, and R_{p2} the charge transfer resistance of the substrate–coating interface.

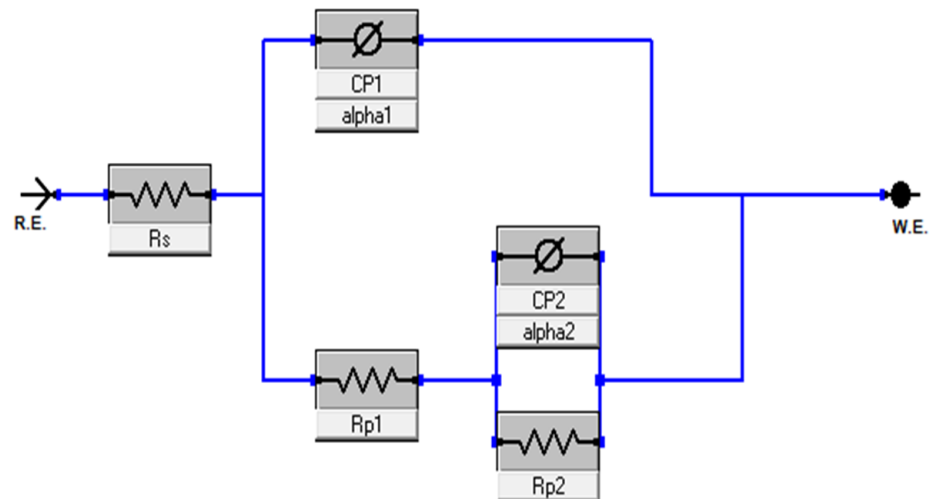


Figure 7. Equivalent circuit to model the behavior of the $\text{Bi}_{3.75}\text{La}_{0.25}\text{Ti}_3\text{O}_{12}$ and $\text{Bi}_3\text{La}_1\text{Ti}_3\text{O}_{12}$ coatings.

Tables 4 and 5 show the values of the electrochemical parameters of the equivalent electrical circuit in Figure 7 for the $\text{Bi}_{3.75}\text{La}_{0.25}\text{Ti}_3\text{O}_{12}$ and $\text{Bi}_3\text{La}_1\text{Ti}_3\text{O}_{12}$ coatings, respectively. Low values of solution resistance (R_s) are observed in the results due to the contribution of the electrolyte. The values for R_{p2} (resistance to polarization to charge transfer of the substrate–coating interface) of the substrate are lower. This shows that the films act as an anti-corrosive barrier against attack by the electrolytic solution.

Table 4. Values of the electrochemical parameters of the equivalent electrical circuit for $\text{Bi}_{3.75}\text{La}_{0.25}\text{Ti}_3\text{O}_{12}$ coatings.

Temperature (°C)	R_s ($\Omega \text{ cm}^2$)	CPE_1 ($\mu\text{F cm}^{-2} \text{ s}^{-(1-\alpha_1)}$)	α_1	R_{p1} ($\Omega \text{ cm}^2$)	CPE_2 ($\mu\text{F cm}^{-2} \text{ s}^{-(1-\alpha_2)}$)	α_2	R_{p2} ($10^3 \Omega \text{ cm}^2$)
700	4.10 (0.3%)	92.56 (4%)	0.75	19.20 (3%)	342.83 (3%)	0.79	2.43 (0.2%)
850	5.24 (0.2%)	87.12 (4%)	0.69	5.31 (2%)	546.23 (3%)	0.75	1.02 (0.3%)
1000	5.91 (0.3%)	92.53 (5%)	0.74	2.84 (2%)	653.76 (4%)	0.67	0.05 (0.2%)

Table 5. Values of the electrochemical parameters of the equivalent electrical circuit for $\text{Bi}_3\text{La}_1\text{Ti}_3\text{O}_{12}$ coatings.

Temperature (°C)	R_s ($\Omega \text{ cm}^2$)	CPE_1 ($\mu\text{F cm}^{-2} \text{ s}^{-(1-\alpha_1)}$)	α_1	R_{p1} ($\Omega \text{ cm}^2$)	CPE_2 ($\mu\text{F cm}^{-2} \text{ s}^{-(1-\alpha_2)}$)	α_2	R_{p2} ($10^3 \Omega \text{ cm}^2$)
700	1.31 (0.4%)	121.05 (2%)	0.54	5.3 (0.1%)	564.21 (3%)	0.56	0.08 (0.01%)
850	3.22 (0.6%)	243.13 (3%)	0.59	2.3 (0.2%)	853.28 (2%)	0.67	0.04 (0.02%)
1000	2.54 (0.6%)	322.25 (3%)	0.64	1.3 (0.3%)	1035.25 (2%)	0.64	0.01 (0.02%)

3.3. X-ray Diffraction

Figures 8 and 9 represent the diffraction pattern obtained for lanthanum bismuth titanate thin films deposited on Hastelloy X substrates. The results were compared with the Joint Committee on Powder Diffraction Standards (JCPDS 73-2128) [32,33]. The effect of temperature on the crystallinity of the coatings was studied. For this purpose, the samples were evaluated at room temperature (25 °C), 700 °C, 850 °C, and 1000 °C. The thin films present diffraction planes mainly at (118) (262), Figure 8, and with less intensity at (317), Figure 9, belonging to the orthorhombic crystalline system.

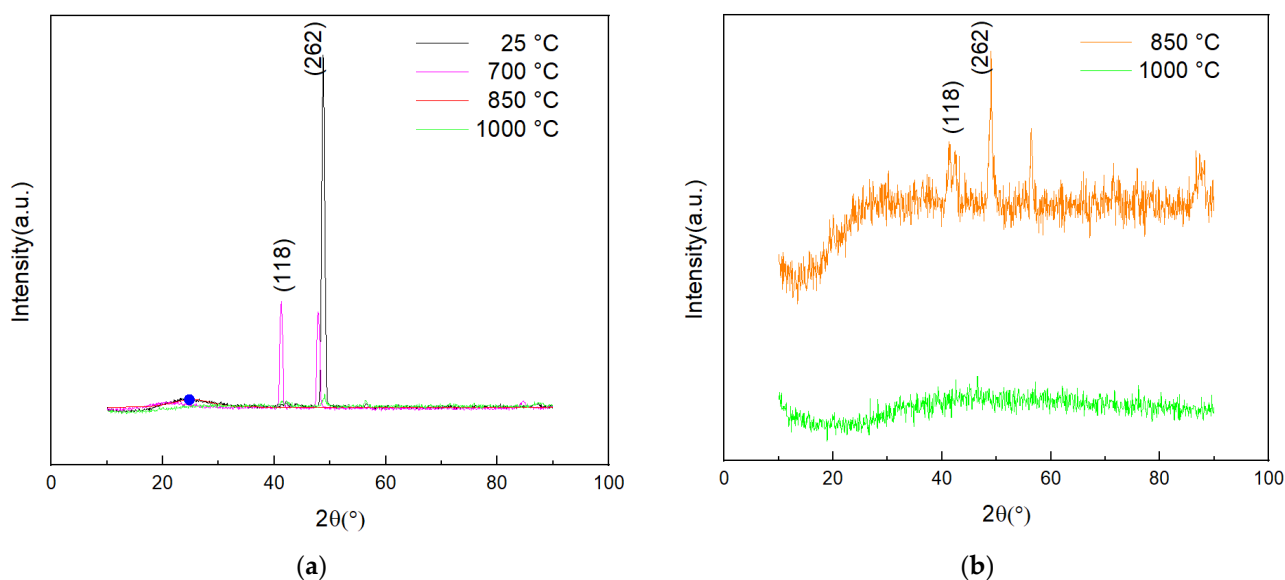


Figure 8. X-ray diffraction patterns for the $\text{Bi}_{3.75}\text{La}_{0.25}\text{Ti}_3\text{O}_{12}$ coatings. (a) All study temperatures, (b) details for temperatures of 850 °C and 1000 °C.

Figures 8 and 9 show that for temperatures of 1000 °C, coatings $\text{Bi}_{3.75}\text{La}_{0.25}\text{Ti}_3\text{O}_{12}$ and $\text{Bi}_3\text{La}_1\text{Ti}_3\text{O}_{12}$ are amorphous. At 850 °C, coating $\text{Bi}_3\text{La}_1\text{Ti}_3\text{O}_{12}$ shows a crystalline structure in the crystallographic plane (317). However, at this same temperature, the thin films $\text{Bi}_{3.75}\text{La}_{0.25}\text{Ti}_3\text{O}_{12}$ are entirely amorphous. Due to the heating temperature, the crystalline phases were observed, possibly due to the corrosive salts' evaporation. Consequently, the high-temperature corrosion influenced the crystallization orientation due to changes in the crystalline planes in the coating. Furthermore, the effect of the element lanthanum as a dopant was evident, since, at 1000 °C, the crystallization of the film usually occurs if thermal annealing is adopted, whereas the composite with a lower amount of lanthanum generated a high quantity of amorphous phase [34].

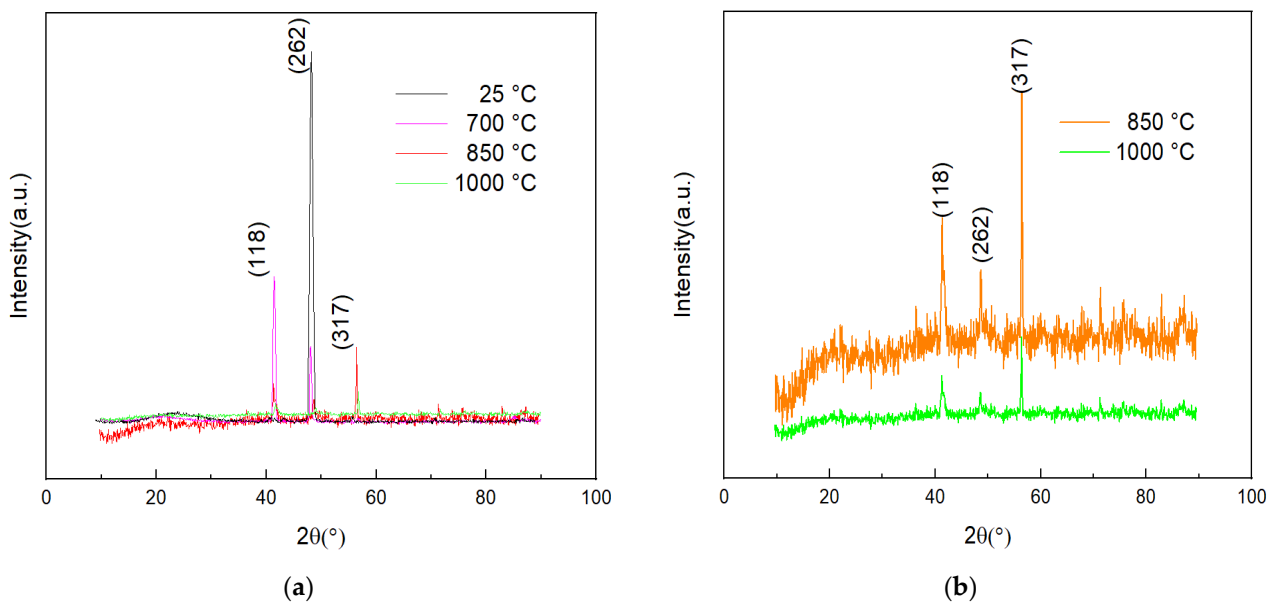


Figure 9. X-ray diffraction patterns for the $\text{Bi}_3\text{La}_1\text{Ti}_3\text{O}_{12}$ coatings. (a) All study temperatures, (b) details for temperatures of 850 °C and 1000 °C.

3.4. Transmission Electron Microscopy

Figure 10a,b are images obtained by transmission electron microscopy of the cross-section of the $\text{Bi}_{3.75}\text{La}_{0.25}\text{Ti}_3\text{O}_{12}$ and $\text{Bi}_3\text{La}_1\text{Ti}_3\text{O}_{12}$ films, respectively. The results confirm the growth of a columnar structure due to the intense atomic bombardment. In addition, good adhesion of the coatings to the substrate is also observed.

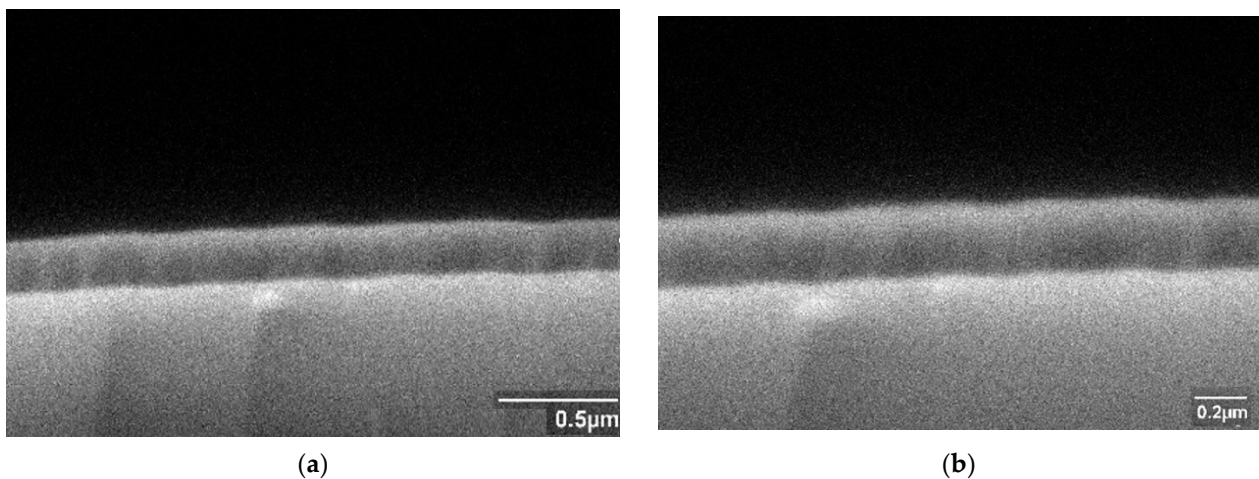


Figure 10. Micrographs were obtained via transmission electron microscopy. (a) $\text{Bi}_{3.75}\text{La}_{0.25}\text{Ti}_3\text{O}_{12}$ film and (b) $\text{Bi}_3\text{La}_1\text{Ti}_3\text{O}_{12}$ film.

3.5. Scanning Electron Microscopy

Figure 11 shows the surface characterization via scanning electron microscopy of the $\text{Bi}_{3.75}\text{La}_{0.25}\text{Ti}_3\text{O}_{12}$ and $\text{Bi}_3\text{La}_1\text{Ti}_3\text{O}_{12}$ coatings as a function of the sintering temperature. In the $\text{Bi}_{3.75}\text{La}_{0.25}\text{Ti}_3\text{O}_{12}$ coatings, rough surfaces are evident due to the sputtering process when forming the coatings. The presence of pores of varied sizes is also evident. In the $\text{Bi}_3\text{La}_1\text{Ti}_3\text{O}_{12}$ coatings, the surface is more homogeneous, and the presence of pores is not evident.

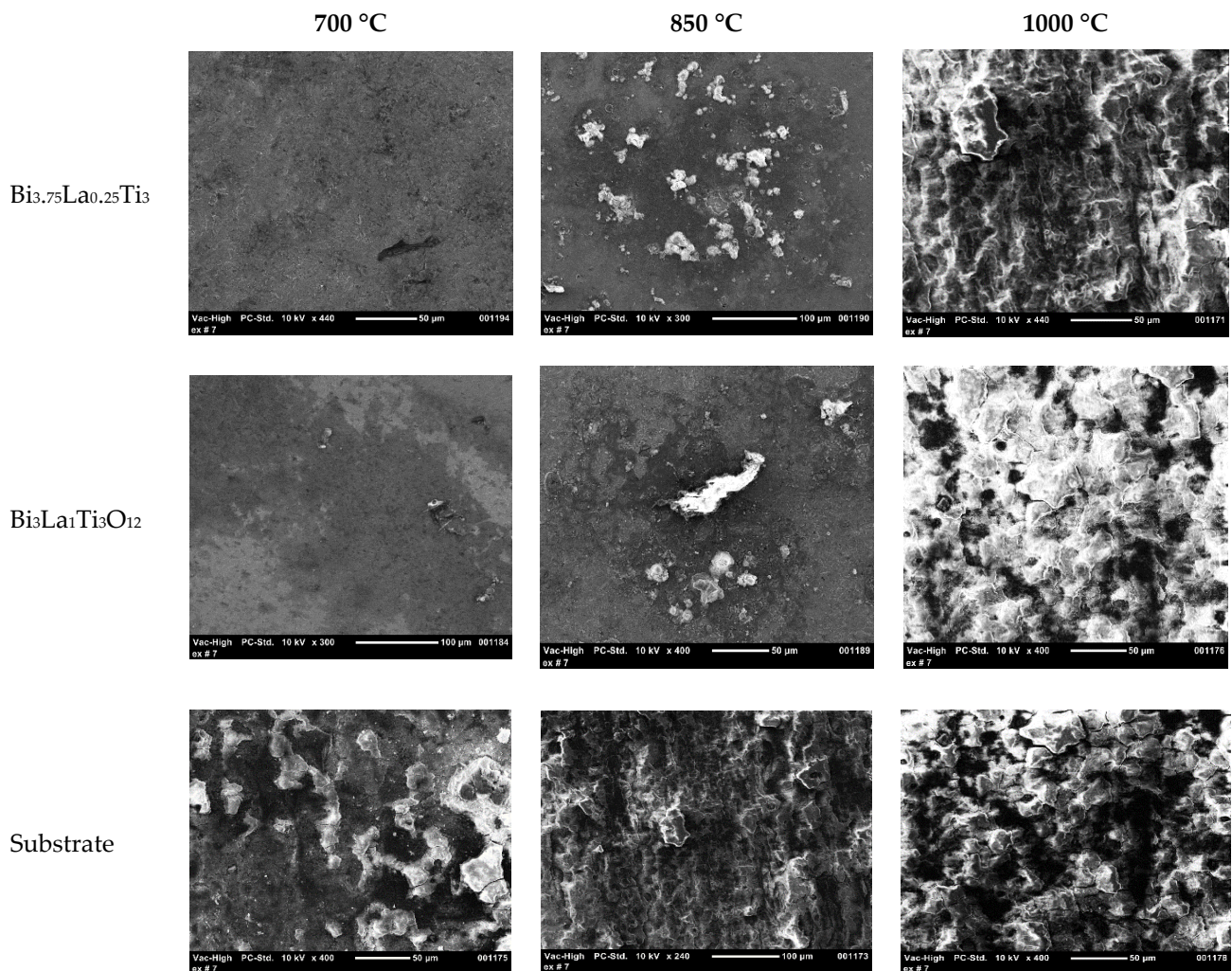


Figure 11. Micrographs via scanning electron microscopy for the $\text{Bi}_{3.75}\text{La}_{0.25}\text{Ti}_3\text{O}_{12}$ and $\text{Bi}_3\text{La}_1\text{Ti}_3\text{O}_{12}$ films.

Figure 11 shows the micrographs of the $\text{Bi}_{3.75}\text{La}_{0.25}\text{Ti}_3\text{O}_{12}$ and $\text{Bi}_3\text{La}_1\text{Ti}_3\text{O}_{12}$ films deposited on the steel. The micrograph represents the specimen with the highest lanthanum content, where deterioration is observed in the central and lower region. However, part of the coating was not affected, as seen in the upper part of the micrograph. For the $\text{Bi}_{3.75}\text{La}_{0.25}\text{Ti}_3\text{O}_{12}$ film, it can be observed that the percentage of lanthanum is 0.25. It can be seen that the films are heterogeneous; they present some discontinuities, such as pores (dark regions) [35]. Homogeneity is evidenced in the micrographs of the films with higher lanthanum content and higher intensity values in the X-ray diffraction. Unlike the films with lower lanthanum content, the micrographs of the films deposited under the same conditions but varying the amount of lanthanum on steel substrates also showed the same Miller indices. However, they decreased intensity, allowing greater amorphism for the system with lower lanthanum. Figure 11 shows the presence of pores and partial detachment of the coating at 1000 °C, so the coatings are distinguished as compromised. It is observed that the behavior against the attack generated by the electrolyte at the time of the evaluation of the corrosion resistance will be lower for the film with lower lanthanum content. As obtained in the electrochemical tests, these systems are 10 times more susceptible to corrosion damage at high temperatures [36].

The elemental chemical analysis was developed for the two types of coatings. The analyzed areas correspond to the micrographs observed in Figure 11. The results found are recorded in Tables 6–8.

Table 6. Chemical analysis for $\text{Bi}_{3.75}\text{La}_{0.25}\text{Ti}_3\text{O}_{12}$ and $\text{Bi}_3\text{La}_1\text{Ti}_3\text{O}_{12}$ coatings and the substrate at a temperature of 700 °C.

System	C	O	Na	Si	S	La	Ti	Cr	Mn	Fe	Ni	V	Bi
	(%)												
Substrate	1	16	4	3	6	0	0	14	3	39	4	10	0
$\text{Bi}_{3.75}\text{La}_{0.25}\text{Ti}_3\text{O}_{12}$	1	15	1	2	1	6	18	7	1	10	5	8	25
$\text{Bi}_3\text{La}_1\text{Ti}_3\text{O}_{12}$	2	13	1	2	1	9	19	8	1	9	5	7	23

Table 7. Chemical analysis for $\text{Bi}_{3.75}\text{La}_{0.25}\text{Ti}_3\text{O}_{12}$ and $\text{Bi}_3\text{La}_1\text{Ti}_3\text{O}_{12}$ coatings and the substrate at a temperature of 850 °C.

System	C	O	Na	Si	S	La	Ti	Cr	Mn	Fe	Ni	V	Bi
	(%)												
Substrate	1	22	4	1	2	0	0	4	1	49	5	16	0
$\text{Bi}_{3.75}\text{La}_{0.25}\text{Ti}_3\text{O}_{12}$	3	19	14	2	4	3	14	2	0	4	5	21	12
$\text{Bi}_3\text{La}_1\text{Ti}_3\text{O}_{12}$	4	18	12	1	5	4	16	1	0	7	1	19	12

Table 8. Chemical analysis for $\text{Bi}_{3.75}\text{La}_{0.25}\text{Ti}_3\text{O}_{12}$ and $\text{Bi}_3\text{La}_1\text{Ti}_3\text{O}_{12}$ coatings and the substrate at a temperature of 1000 °C.

System	C	O	Na	Si	S	La	Ti	Cr	Mn	Fe	Ni	V	Bi
	(%)												
Substrate	1	18	2	1	2	0	0	2	1	46	2	25	0
$\text{Bi}_{3.75}\text{La}_{0.25}\text{Ti}_3\text{O}_{12}$	1	22	16	1	2	2	12	0	0	2	1	29	12
$\text{Bi}_3\text{La}_1\text{Ti}_3\text{O}_{12}$	1	25	19	2	1	1	11	0	0	2	1	22	15

In the chemical analysis, elements such as Ti, Bi, and O are evident, which correspond to the films. In addition, elements such as the substrate's Cr, Fe, and Ni components are also reported.

3.6. Energy Activation

In general, the estimate of the activation energy is determined by the Arrhenius equation. This study used three temperatures of 700 °C, 850 °C, and 1000 °C. Activation energies were 193 kJ/mol for the substrate, 69.8 kJ/mol for films of the $\text{Bi}_{3.75}\text{La}_{0.25}\text{Ti}_3\text{O}_{12}$ system, and 87.3 kJ/mol for $\text{Bi}_3\text{La}_1\text{Ti}_3\text{O}_{12}$ coatings. The variation in the activation energy values results is related to the effect of the concentrations of lanthanum that make up the coatings.

4. Conclusions

The corrosion rate was determined to have a direct relationship with the temperature because the mechanisms induced by the Na_2SO_4 and V_2O_5 salts have generated condensation. Therefore, increasing the temperature increases the corrosion current density in the thin films of $\text{Bi}_{3.75}\text{La}_{0.25}\text{Ti}_3\text{O}_{12}$ and $\text{Bi}_3\text{La}_1\text{Ti}_3\text{O}_{12}$. Furthermore, by comparing the two compounds, it is determined that the increase in La alters the positive acid character, thus decreasing the dissolution of the oxides and increasing the protection.

The potentiodynamic polarization curves for the coatings determined minimal damage for a temperature of 700 °C—the damage increases as a function of the sintering temperature of the thin films. However, at 1000 °C, the damage is catastrophic due to the increased corrosion current density. In addition, the existence of general dissolution in the anodic region was determined in the two systems studied.

The films have crystalline characteristics that are preserved up to 850 °C. However, for the coating with higher lanthanum content, a structure is obtained up to 1000 °C, owing

to the generated phases. Once cooled, the coating is affected. Amorphous processes are generated due to the increase in corrosion current density.

Homogeneity is evidenced in the micrographs of the films with higher lanthanum content and higher intensity values in the X-ray diffraction.

The results of the activation energy values are related to the effect of the concentrations of lanthanum that make up the coatings.

The results allowed us to establish that the $\text{Bi}_3\text{La}_1\text{Ti}_3\text{O}_{12}$ coatings evaluated at temperatures of 700 °C, 850 °C, and 1000 °C exhibit better stability at relatively high temperatures.

Author Contributions: Conceptualization, W.A. and J.B.-R.; methodology, J.S.-M.; software, W.A.; validation, J.B.-R.; formal analysis, J.S.-M.; investigation, W.A. and J.B.-R. All authors have read and agreed to the published version of the manuscript.

Funding: This research work was funded by Vicerrectoria de Investigaciones Universidad Militar Nueva Granada through the IMP ING 3123 vigencia 2020–2021.

Institutional Review Board Statement: Not applicable.

Data Availability Statement: Not applicable.

Acknowledgments: W. Aperador acknowledges the Vicerrectoría de Investigaciones Universidad Militar Nueva Granada through the IMP ING 3123 vigencia 2020–2021.

Conflicts of Interest: The authors declare no conflict of interest.

References

1. Grao, M.; Redfern, J.; Kelly, P.J.; Ratova, M. Magnetron co-sputtered $\text{Bi}_{12}\text{TiO}_{20}/\text{Bi}_4\text{Ti}_3\text{O}_{12}$ composite—An efficient photocatalytic material with photoinduced oxygen vacancies for water treatment application. *Appl. Surf. Sci.* **2021**, *552*, 149486. [[CrossRef](#)]
2. Das, K.; Bariki, R.; Majhi, D.; Mishra, A.; Das, K.K.; Dhiman, R.; Mishra, B.G. Facile synthesis and application of $\text{CdS}/\text{Bi}_{20}\text{TiO}_{32}/\text{Bi}_4\text{Ti}_3\text{O}_{12}$ ternary heterostructure: A synergistic multi-heterojunction photocatalyst for enhanced endo-sulfan degradation and hydrogen evolution reaction. *Appl. Catal. B* **2022**, *303*, 120902. [[CrossRef](#)]
3. Wang, L.; Ma, W.; Fang, Y.; Zhang, Y.; Jia, M.; Li, R.; Huang, Y. $\text{Bi}_4\text{Ti}_3\text{O}_{12}$ Synthesized by High Temperature Solid Phase Method and its Visible Catalytic Activity. *Procedia Environ. Sci. Eng. Manag.* **2013**, *18*, 547–558. [[CrossRef](#)]
4. Lin, C.; Ma, J.; Yi, F.; Zhang, H.; Qian, Y.; Zhang, K. Ag NPs modified plasmonic Z-scheme photocatalyst $\text{Bi}_4\text{Ti}_3\text{O}_{12}/\text{Ag}/\text{Ag}_3\text{PO}_4$ with improved performance for pollutants removal under visible light irradiation. *Ceram. Int.* **2020**, *46*, 14650–14661. [[CrossRef](#)]
5. Wang, W.; Zheng, K.; Sun, S.; Qin, L.; Tang, L.; Li, Z. One-step synthesis of $\text{Bi}_4\text{Ti}_3\text{O}_{12}/\text{Bi}_2\text{O}_3/\text{Bi}_{12}\text{TiO}_{20}$ spherical ternary heterojunctions with enhanced photocatalytic properties via sol-gel method. *Solid State Sci.* **2020**, *100*, 106098. [[CrossRef](#)]
6. Wang, W.; Zheng, K.; Sun, S.; Qin, L.; Tang, L.; Li, Z. Characterization of the full matrix constants of $\text{Bi}_4\text{Ti}_3\text{O}_{12}$ ceramics. *Ceram. Int.* **2021**, *47*, 23518–23527. [[CrossRef](#)]
7. Caicedo, J.C.; Zambrano, G.; Aperador, W.; Escobar-Alarcon, L.; Camps, E. Mechanical and electrochemical characterization of vanadium nitride (VN) thin film. *Appl. Surf. Sci.* **2011**, *258*, 312–320. [[CrossRef](#)]
8. Piedrahita, W.F.; Aperador, W.; Caicedo, J.C.; Prieto, P. Evolution of physical properties in hafnium carbonitride thin films. *J. Alloys Compd.* **2017**, *690*, 485–496. [[CrossRef](#)]
9. Macías, H.A.; Yate, L.; Coy, L.E.; Aperador, W.; Olaya, J.J. Influence of Si-addition on wear and oxidation resistance of TiWSi_xN thin films. *Ceram. Int.* **2019**, *45*, 17363. [[CrossRef](#)]
10. Amaya, C.; Aperador, W.; Caicedo, J.C.; Espinoza-Beltrán, F.J.; Muñoz-Saldaña, J.; Zambrano, G.; Prieto, P. Corrosion study of Alumina/Yttria-Stabilized Zirconia ($\text{Al}_2\text{O}_3/\text{YSZ}$) nanostructured Thermal Barrier Coatings (TBC) exposed to high temperature treatment. *Corros. Sci.* **2009**, *51*, 2994–2999. [[CrossRef](#)]
11. Liu, C.; Xiao, C.; Xie, C.; Li, W. Flexible organic solar cells: Materials, large-area fabrication techniques and potential applications. *Nano Energy* **2021**, *89*, 106399. [[CrossRef](#)]
12. Zhang, M.; Jeerh, G.; Zou, P.; Lan, R.; Wang, M.; Wang, H.; Tao, S. Recent development of perovskite oxide-based electrocatalysts and their applications in low to intermediate temperature electrochemical devices. *Mater. Today* **2021**, *49*, 351–359. [[CrossRef](#)]
13. Song, D.; Song, T.; Paik, U.; Lyu, G.; Kim, J.; Yang, S.; Jung, Y. Hot-corrosion resistance and phase stability of $\text{Yb}_2\text{O}_3\text{-Gd}_2\text{O}_3\text{-Y}_2\text{O}_3$ stabilized zirconia-based thermal barrier coatings against $\text{Na}_2\text{SO}_4 + \text{V}_2\text{O}_5$ molten salts. *Surf. Coat. Technol.* **2020**, *400*, 126197. [[CrossRef](#)]
14. Yate, L.; Coy, L.E.; Aperador, W. Robust tribo-mechanical and hot corrosion resistance of ultra-refractory Ta-Hf-C ternary alloy films. *Sci. Rep.* **2017**, *7*, 3080. [[CrossRef](#)]
15. Kim, K.Y.; Yoon, D.J. Site Preference of La in $\text{Bi}_{3.75}\text{La}_{0.25}\text{Ti}_3\text{O}_{12}$ Using Neutron Powder Diffraction and Raman Scattering. *J. Electroceram.* **2005**, *14*, 265–271. [[CrossRef](#)]
16. Perez, F.J.; Hierro, M.P.; Dudley, D.; Gomez, C.; Romero, M.; Daza, L. Hot-corrosion studies of separator plates of Aisi-310 stainless steels in molten-carbonate fuel cells. *Oxid. Met.* **2000**, *53*, 375–398. [[CrossRef](#)]

17. Zeng, C.L.; Guo, P.Y.; Wu, W.T. Electrochemical impedance spectra for the corrosion of two-phase Cu–15Al alloy in eutectic (Li, K)₂CO₃ at 650 °C in air. *Electrochim. Acta* **2004**, *49*, 1445–1450. [[CrossRef](#)]
18. Ni, C.S.; Lu, L.Y.; Zeng, C.L.; Niu, Y. Electrochemical impedance studies of the initial-stage corrosion of 310S stainless steel beneath thin film of molten (0.62Li,0.38K)₂CO₃ at 650 °C. *Corros. Sci.* **2011**, *53*, 1018–1024. [[CrossRef](#)]
19. Shi, X.; Wang, Y.; Li, H.; Zhang, S.; Zhao, R.; Li, G.; Zhang, R.; Sheng, Y.; Cao, S.; Zhao, Y.; et al. Corrosion resistance and biocompatibility of calcium-containing coatings developed in near-neutral solutions containing phytic acid and phosphoric acid on AZ31B alloy. *J. Alloys Compd.* **2020**, *823*, 153721. [[CrossRef](#)]
20. Li, J.; Shi, H.; Liu, F.; Han, E. Self-healing epoxy coating based on tung oil-containing microcapsules for corrosion protection. *Prog. Org. Coat.* **2021**, *156*, 106236. [[CrossRef](#)]
21. Feng, J.; Ming-Wang, Z.; Zheng, D.; Song, G.-L. Influence of dissolved oxygen on the corrosion of mild steel in a simulated cement pore solution under supercritical carbon dioxide. *Constr. Build. Mater.* **2021**, *311*, 125270. [[CrossRef](#)]
22. David, C.; Ruel, F.; Boissy, C.; Roche, V.; Véron, M.; Nogueira, R.P. On the effect of plastic pre-straining on the corrosion behaviour of a duplex stainless steel and how the emergence of slip steps affects the hydrogen evolution reaction kinetics. *Corros. Sci.* **2020**, *179*, 109167. [[CrossRef](#)]
23. Liu, Y.; Cheng, W.; Liu, Y.; Niu, X.; Wang, H.; Cui, L.W. Effect of alloyed Ca on the microstructure and corrosion behavior of extruded Mg–Bi–Al-based alloys. *Mater. Character.* **2020**, *163*, 110292. [[CrossRef](#)]
24. Yuan, G.; Zhang, G.; Li, K.; Li, F.; Cao, Y.; He, J.; Huang, Z.; Jia, Q.; Zhang, S.; Zhang, H. Preparation and Photocatalytic Performance for Degradation of Rhodamine B of AgPt/Bi₄Ti₃O₁₂ Composites. *Nanomaterials* **2020**, *10*, 2206. [[CrossRef](#)]
25. Thilagavathi, R.; Prithiba, A.; Rajalakshmi, R. Assessment of *Passiflora vitifolia* Leaves Extract as a Potential Inhibitor for Mild Steel Acid Corrosion. *Rasayan J. Chem.* **2019**, *12*, 431–449. [[CrossRef](#)]
26. Bautista, A.; González-Centeno, A.; Blanco, G.; Guzmán, S. Application of EIS to the study of corrosion behaviour of sintered ferritic stainless steels before and after high-temperature exposure. *Mater. Character.* **2008**, *59*, 32–39. [[CrossRef](#)]
27. Encinas-Sánchez, V.; de Miguel, M.T.; Lasanta, M.I.; García-Martín, G.; Pérez, F.J. Electrochemical impedance spectroscopy (EIS): An efficient technique for monitoring corrosion processes in molten salt environments in CSP application. *Sol. Energy Mater. Sol. Cells* **2019**, *191*, 157–163. [[CrossRef](#)]
28. Lario, J.; Escuder, A.; Segovia, F.; Amigó, V. Electrochemical corrosion behavior of Ti–35Nb–7Zr–5Ta powder metallurgical alloys after Hot Isostatic Process in fluorinated artificial saliva. *J. Mater. Res. Technol.* **2022**, *16*, 1435–1444. [[CrossRef](#)]
29. Sun, L.; Fu, Q.; Sun, J.; Zhang, G. Comparison investigation of hot corrosion exposed to Na₂SO₄ salt and oxidation of MoSi₂-based coating on Nb alloy at 100 °C. *Surf. Coat. Technol.* **2020**, *385*, 125388. [[CrossRef](#)]
30. Operator, W.; Bautista-Ruiz, J.; Caicedo, J. Synergistic corrosion-wear effect in austenitic powder metallurgical steel with different titanium additions. *Rasayan J. Chem.* **2022**, *15*, 57–64.
31. Hernández-Cuevas, G.; Leyva Mendoza, J.R.; García-Casillas, P.E.; Olivas-Armendariz, I.; Mani-González, P.G.; Díaz de la Torre, S. Synthesis and characterization of niobium doped bismuth titanate. *Boletín de la Sociedad Española de Cerámica y Vidrio* **2021**, *in press*. [[CrossRef](#)]
32. Nogueira, A.E.; Lima, A.R.F.; Longo, E.; Leite, E.R.; Camargo, E. Effect of lanthanum and lead doping on the microstructure and visible light photocatalysis of bismuth titanate prepared by the oxidant peroxide method (OPM). *J. Photochem. Photobiol. A* **2015**, *312*, 55–63. [[CrossRef](#)]
33. Simões, A.Z.; Piano, R.F.; Riccardi, C.S.; Cavalcante, L.S.; Longo, E.; Varela, J.A. Dielectric properties of pure and lanthanum modified bismuth titanate thin films. *J. Alloys Compd.* **2008**, *454*, 66–71. [[CrossRef](#)]
34. Liu, Y.; Jiang, H.; Zhao, X.; Deng, X.; Zhang, W. High temperature electrical insulation and adhesion of nanocrystalline YSZ/Al₂O₃ composite film for thin-film thermocouples on Ni-based superalloy substrates. *Appl. Surf. Sci.* **2022**, *579*, 152169. [[CrossRef](#)]
35. Obitte, B.C.N.; Ikhioya, I.L.; Whyte, G.M.; Chime, U.K.; Ezekoye, B.A.; Ekwealor, A.B.C.; Maaza, M. The effects of doping and temperature on properties of electrochemically deposited Er³⁺ doped ZnSe thin films. *Opt. Mater.* **2022**, *124*, 111979. [[CrossRef](#)]
36. Ganesha Krishna, V.S.; Mahesha, M.G. Influence of the substrate temperature on the structural, optical, and morphological properties of (101) oriented ZnSe thin films for window applications in solar cells. *Mater. Today* **2022**, *58*, 623–626.